OPEN ACCESS
IOP Publishing | International Atomic Energy Agency
Nuclear Fusion
Nucl. Fusion **67** (2027) 016018 (14pp)
https://doi.org/10.1088/1741-4326/aeb431

Icosahedral-group beam layouts for highly uniform direct-drive laser fusion

Atsushi Sunahara*, Gaurav Raj, Trevor Cohen, P. Morgan Pattison and Shuji Nakamura

Blue Laser Fusion, Inc., Goleta, CA, United States of America

E-mail: asunahara@bluelaserfusion.com

Received 27 May 2026, revised 30 September 2026
Accepted for publication 14 October 2026
Published 30 October 2026



Abstract

We investigate irradiation uniformity in direct-drive laser fusion using beam layouts generated from the full rotational icosahedral group. By expanding the incident intensity in spherical harmonics, we show the selection rules imposed by exact icosahedral invariance and identify the forbidden multipole degrees. These exclusions are independent of the single-beam profile and therefore remain valid for both delta-function and finite-width beams. Using flat-top and von Mises–Fisher beam profiles, we evaluate the resulting root-mean-square nonuniformity and compare an optimized 60-beam icosahedral layout with the conventional OMEGA 60-beam geometry. For smooth beam profiles, this model predicts substantially lower nonuniformity for the optimized icosahedral layout than for the OMEGA-60 geometry, because exact low-degree cancellation is combined with efficient high-degree attenuation by the beam-profile transfer coefficients. We further examine random beam-weight imbalance and show that optimized high-beam-count icosahedral layouts remain robust over the range studied. These results establish a symmetry-based design principle for low-mode control and improved irradiation uniformity in direct-drive laser implosions.

Keywords: direct-drive laser fusion, irradiation uniformity, icosahedral group, spherical harmonics, beam layout optimization

(Some figures may appear in colour only in the online journal)

1. Introduction

Highly uniform spherical drive symmetry is a fundamental requirement for laser inertial confinement fusion [1–3]. Irradiation nonuniformity seeds hydrodynamic instabilities, distorts implosion symmetry, reduces stagnation pressure, and degrades ignition and burn performance. Achieving uniform drive with a finite number of beams, therefore, requires solving a fundamental geometric problem. For certain small beam numbers, highly symmetric configurations derived from regular polyhedra provide natural candidates. In the general case, however, the problem becomes one of optimal point distribution on the sphere. It is closely related to the Thomson problem, one of the classical formulations of discrete point optimization on the sphere [4, 5].

From this perspective, beam layout in laser inertial fusion is not merely an engineering choice, but a physically constrained spherical optimization problem. This perspective provides a natural framework for appreciating the appeal of illumination schemes based on regular polyhedra, specifically the regular icosahedron in this paper, and for extending them to practical beam configurations.

Because direct-drive implosions are intrinsically spherical, the angular distribution of the incident drive intensity $I(\Omega)$ on the capsule surface is naturally described as a function defined on the unit sphere, where Ω specifies a direction on the sphere.

* Author to whom any correspondence should be addressed.

Original content from this work may be used under the terms of the Creative Commons Attribution 4.0 licence. Any further distribution of this work must maintain attribution to the author(s) and the title of the work, journal citation and DOI.

 © 2026 The Author(s). Published by IOP Publishing Ltd on behalf of the IAEA

It is expanded in spherical harmonics,

$$I(\Omega) = \sum_{\ell=0}^{\infty} \sum_{m=-\ell}^{\ell} a_{\ell m} Y_\ell^m(\Omega), \tag{1}$$

where Y_ℓ^m form an orthonormal basis on the unit sphere with degree ℓ and order m, and $a_{\ell m}$ are the corresponding expansion coefficients. The degree ℓ characterizes the angular scale. Small values of ℓ correspond to long-wavelength distortions of the drive, while larger values represent progressively finer angular structure. The coefficient with $\ell = 0$ represents the uniform component of the drive and equals its spherical average intensity. Coefficients with $\ell \geqslant 1$ quantify deviations from perfect symmetry.

For each degree ℓ, we define the angular power

$$\mathcal{P}_\ell = \sum_{m=-\ell}^{\ell} |a_{\ell m}|^2. \tag{2}$$

It measures the total strength of asymmetry at that angular scale. The root-mean-square (RMS) nonuniformity, $\sigma_{\rm rms}$, is then defined as

$$\sigma_{\rm rms}^2 = \frac{\sum_{\ell \geqslant 1} \mathcal{P}_\ell}{a_{00}^2}, \tag{3}$$

i.e. the total power in all nonzero spherical-harmonic degrees normalized to the squared monopole component. This spectral representation reveals a natural hierarchy in spherical implosions. Low-degree asymmetries couple directly to global deceleration dynamics and stagnation geometry, whereas higher-degree modes can degrade performance through hydrodynamic instability growth and mixing. Both low- and high-degree components, therefore, influence fusion performance through distinct physical pathways.

Low-degree asymmetry is a well-recognized performance limiter in ignition-regime experiments at the National Ignition Facility (NIF). Simulations show that low-order flux asymmetries degrade stagnation and reduce yield, while experiments demonstrate a clear sensitivity of implosion performance to low-mode distortions and symmetry tuning [6–10].

In direct drive, beam geometry is directly linked to low-degree drive structure, because the long-wavelength nonuniformity is governed mainly by the angular distribution of beam axes and their relative powers. At the OMEGA laser facility [11–14], diagnostics and simulations have shown that low-degree asymmetries can strongly limit cryogenic implosion performance [15, 16]. Simulations including smoothing by spectral dispersion and cross-beam energy transfer (CBET) further show that coherent low-degree components may persist, or arise from global system-level interactions, even when higher-degree structure is partially smoothed [17]. Therefore, reducing the overall $\sigma_{\rm rms}$ and suppressing low-degree spectral power are complementary but distinct requirements for high-performance direct-drive implosions [18].

Laser–plasma-interaction effects further couple drive nonuniformity to implosion performance through CBET and nonuniform absorption. Measurements on OMEGA and NIF direct-drive implosions show that CBET modifies angularly resolved mass-ablation rates and ablation-front trajectories [19], while unabsorbed-light diagnostics indicate that absorption in OMEGA implosions is less uniform than previously assumed [20]. Recent direct-drive-relevant CBET simulations likewise show that energy transfer between crossing beams can redistribute laser energy and inhibit implosion performance [21, 22].

A key step in the theoretical analysis of irradiation uniformity was the analysis of Skupsky and Lee [11], who separated the nonuniformity into a single-beam factor and a purely geometrical factor determined only by the beam directions and weights. Their formulation made explicit that low-degree spectral content is governed predominantly by beam geometry and showed that suitable angular arrangements can suppress selected low-degree modes. Schmitt showed, in an idealized setting, that absolutely uniform illumination of a laser-fusion pellet can be obtained when the single-beam energy-deposition profile is appropriately shaped on the target sphere with suitable beam directions [23]. McGeoch and Obenschain optimized beam configurations based on Schmitt's framework using approximate hyper-Gaussian profiles [24]. Murakami and collaborators also investigated irradiation uniformity through practical mode-resolved studies [25, 26] and electrostatic optimization methods that treat beam directions as mutually repelling points on a sphere, thereby providing a numerical route to near-uniform multibeam configurations [27, 28]. In contrast to the specific profile requirement in Schmitt's construction, our framework ensures that symmetry-forbidden spherical-harmonic degrees cancel for any common axisymmetric beam profile, provided that the beams within each complete icosahedral orbit have equal weights.

A complementary strategy is embodied in the StarDriver concept, which reduces global $\sigma_{\rm rms}$ through beamlet multiplication and strong spatial and temporal incoherence [29–31]. Such statistical smoothing is effective against high-degree structure, but systematic suppression of low-degree modes requires structural control of the angular beam distribution. Our previous paper [32] presented the concept of a direct-drive laser fusion reactor employing high beam counts above about 500 in order to improve irradiation uniformity. However, that work did not quantitatively evaluate the irradiation uniformity of the beam layout itself, nor did it examine the present symmetry-based spectral structure of the irradiation nonuniformity. Specifically, the present paper (i) clarifies how icosahedral symmetry constrains the allowed and forbidden multipole orders of the irradiation pattern, (ii) quantitatively compares the optimized 60-beam configuration based on the full rotational icosahedral group, denoted Ic_{60}, with the conventional OMEGA 60-beam geometry, denoted Ω_{60}, and (iii) evaluates the robustness of optimized high-beam-count icosahedral configurations, denoted Ic_N, against random beam-weight imbalance as the total beam number N increases. In the present idealized irradiation model, the resulting nonuniformity reaches levels comparable to, or lower than, values often regarded as important design targets for

ignition-class implosions, while remaining within a direct-drive configuration. This provides a mathematically grounded route to direct-drive configurations with very low calculated irradiation nonuniformity and a scalable design framework for high-beam-count fusion systems.

2. Icosahedral symmetry and spectral selection rules

In this section, we examine how icosahedral symmetry constrains the spherical-harmonic content of the incident beam intensity introduced in section 1. We first recall the low-order cancellation implied by spherical-design theory. We then show that exact rotational icosahedral symmetry imposes a stronger constraint and excludes additional multipole orders beyond the spherical 5-design range. Finally, we show that the same symmetry-based restriction remains valid for finite-width beams and is therefore not limited to the delta-function case.

2.1. Tight spherical 5-design

A direct geometric explanation for the suppression of the lowest-order multipoles is provided by spherical-design theory. The 12 vertices of the regular icosahedron provide a classical example of a tight spherical 5-design on the unit sphere S^2 [5]. Let $\{\Omega_i\}_{i=1}^{12}$ denote the corresponding vertex directions. Because these points form a spherical 5-design, the discrete average over the 12 vertices reproduces the uniform spherical average for all spherical harmonics up to degree $\ell = 5$. One therefore obtains

$$\frac{1}{12}\sum_{i=1}^{12} Y_\ell^m(\Omega_i) = \frac{1}{4\pi}\int_{S^2} Y_\ell^m(\Omega)\,\mathrm{d}\Omega, \qquad (1\leqslant\ell\leqslant 5). \quad (4)$$

Since the spherical average of Y_ℓ^m vanishes for all $\ell\geqslant 1$, it follows immediately that

$$\frac{1}{12}\sum_{i=1}^{12} Y_\ell^m(\Omega_i) = 0, \qquad (1\leqslant\ell\leqslant 5). \quad (5)$$

Therefore, all multipole components up to $\ell = 5$ are eliminated purely by geometry. This argument explains the absence of the lowest-order multipoles, but by itself it does not determine which higher-order modes with $\ell\geqslant 6$ are also excluded. To clarify the full set of forbidden orders, one must use the exact rotational icosahedral symmetry of the beam configuration.

2.2. Exact invariance under the full icosahedral rotation group

The rotational icosahedral group I consists of the 60 proper rotations listed in table 1 [33]. In the equal-weight construction considered here, the beam pattern is generated by applying every element $g \in I$ to a reference beam profile $b(\Omega)$. The total intensity is therefore

Table 1. Conjugacy classes of the rotational icosahedral group I. The group contains 60 proper rotations, which generate the full orbit in equation (6). These rotations define the symmetry operations under which the incident intensity is required to remain invariant [33].

Class	Rotation angle	Number of elements
C_1	0	1
C_2	π	15
C_3	$2\pi/3$	20
C_5	$2\pi/5$	12
C_5^2	$4\pi/5$	12

$$I(\Omega) = \sum_{g\in I} b\left(g^{-1}\Omega\right), \quad (6)$$

where g runs over the full 60-element orbit summarized in table 1. Here, $b(g^{-1}\Omega)$ denotes the reference beam profile b, rotated by the group element g and evaluated at the direction Ω.

Equation (6) makes the symmetry explicit. Rotating the entire configuration by any element of the same group produces no new beams and merely permutes the 60 copies already present in the sum. Because all copies are identical and enter with equal weight, this permutation leaves the total intensity unchanged. The resulting pattern is therefore exactly invariant under the rotational icosahedral group I.

This invariance has an important consequence for the multipole expansion. Rotations do not mix different multipole orders ℓ and only mix the m components within a fixed ℓ. Accordingly, the symmetry constraint can be imposed independently at each degree ℓ. For a given ℓ, the icosahedral rotations act within the $(2\ell+1)$-dimensional space spanned by $\{Y_\ell^m\}_{m=-\ell}^{\ell}$. A nonzero degree-$\ell$ contribution can therefore survive only if this space contains at least one angular pattern that remains unchanged under every rotation in I.

2.3. Allowed and forbidden multipole orders

We denote by $n_A(\ell)$ the dimension of the subspace of degree-ℓ spherical-harmonic patterns that remain invariant under all rotations of I. Equivalently, $n_A(\ell)$ is the multiplicity of the totally symmetric representation in the degree-ℓ spherical-harmonic space. Thus, $n_A(\ell) = 0$ means that no nonzero icosahedrally invariant angular pattern exists at degree ℓ, whereas $n_A(\ell)\geqslant 1$ means that one or more linearly independent invariant patterns are allowed. The previous discussion then immediately implies that, if $n_A(\ell) = 0$, the entire ℓth multipole component must vanish.

Cohan tabulated the multiplicity $n_A(\ell)$ up to $\ell = 15$ in table 8 of [33]. Within that range, $n_A(\ell) = 0$ for $\ell = 1,\ldots,5$, consistent with the spherical 5-design result above, and also for $\ell = 7, 8, 9, 11, 13$, and 14 [33]. The first nontrivial totally symmetric multipole beyond the monopole $\ell = 0$ appears

at $\ell = 6$, for which $n_A(6) = 1$ [33]. Thus, exact icosahedral symmetry excludes additional multipole orders beyond those removed by the 5-design property alone.

For higher degrees, Meyer [34] derived a generating function for the number of linearly independent icosahedrally invariant spherical harmonics at each degree. Let

$$h(t;I) = \sum_{\ell=0}^{\infty} n_A(\ell)\, t^{\ell} \tag{7}$$

denote this generating function, where t is a formal expansion variable. In other words, the coefficient of t^{ℓ} in $h(t;I)$ gives the number of symmetry-allowed degree-ℓ icosahedral harmonics. Meyer showed that, for the rotational icosahedral group I,

$$h(t;I) = \frac{1+t^{15}}{(1-t^{6})(1-t^{10})}. \tag{8}$$

To interpret this expression [34, 35], we use the geometric-series expansion

$$\frac{1}{1-t^{6}} = \sum_{a=0}^{\infty} t^{6a}, \qquad \frac{1}{1-t^{10}} = \sum_{b=0}^{\infty} t^{10b}, \tag{9}$$

so that

$$\frac{1}{(1-t^{6})(1-t^{10})} = \left(\sum_{a=0}^{\infty} t^{6a}\right)\left(\sum_{b=0}^{\infty} t^{10b}\right) = \sum_{a,b\geqslant 0} t^{6a+10b}. \tag{10}$$

Thus, the denominator generates powers only of the form t^{6a+10b}, where a and b are non-negative integers. Multiplication by the numerator $(1+t^{15})$ then produces two branches,

$$\sum_{a,b\geqslant 0} t^{6a+10b} \qquad \text{and} \qquad \sum_{a,b\geqslant 0} t^{15+6a+10b}, \tag{11}$$

so that totally symmetric icosahedral harmonics can occur only for degrees of the form

$$\ell = 6a+10b \quad \text{or} \quad \ell = 15+6a+10b, \quad a,b\geqslant 0. \tag{12}$$

It follows that the next forbidden degrees beyond $\ell = 15$ are $\ell = 17, 19, 23$, and 29, whereas all degrees $\ell \geqslant 30$ are allowed by symmetry. Combining this result with the low-degree classification above, the only degrees for which no totally symmetric icosahedral component exists are

$$\ell = 1,2,3,4,5,7,8,9,11,13,14,17,19,23, \text{and } 29.$$

Accordingly, if the incident intensity is exactly invariant under the rotational icosahedral group generated by the 60 rotations listed in table 1, then all spherical-harmonic coefficients at these forbidden degrees must vanish.

These symmetry constraints depend only on the complete 60-element icosahedral orbit in equation (6), not on the detailed form of the single-beam profile. A finite beam width can modify the amplitudes of symmetry-allowed modes, but it cannot generate a multipole order forbidden by the rotational icosahedral symmetry itself. Therefore, the same excluded degrees apply to delta-function beams as well as to smooth or sharp-edged finite-width beam profiles.

3. Single-beam profile model and transfer coefficients

We consider axisymmetric single-beam angular profiles and their associated transfer coefficients B_ℓ. The beam width is parameterized by a single angular scale θ_{b}. For the flat-top profile, we set $\theta_{\mathrm{b}} \equiv \alpha$, where α is the beam half-angle. For the von Mises–Fisher (vMF) profile [36, 37], θ_{b} is defined by the half-maximum condition $b(\theta_{\mathrm{b}}) = \frac{1}{2}b(0)$. In what follows, both models are expressed in terms of θ_{b}.

Let Ω_0 denote the beam-axis direction. For an axisymmetric beam, the profile depends only on the offset angle γ, defined by $\cos\gamma = \Omega\cdot\Omega_0$, so that $b(\Omega) \equiv b(\gamma)$. We normalize the profile on the sphere as

$$2\pi \int_{-1}^{1} b(\gamma(\mu))\, \mathrm{d}\mu = 1, \qquad \mu = \cos\gamma. \tag{13}$$

The profile then admits the Legendre expansion

$$b(\gamma) = \sum_{\ell=0}^{\infty} \frac{2\ell+1}{4\pi} B_\ell P_\ell(\cos\gamma), \tag{14}$$

where the transfer coefficients are

$$B_\ell = 2\pi \int_{-1}^{1} b(\gamma(\mu))\, P_\ell(\mu)\, \mathrm{d}\mu. \tag{15}$$

With this convention, $B_0 = 1$.

For a discrete set of beam axes Ω_j with weights w_j, the spherical-harmonic coefficients are

$$a_{\ell m} = B_\ell \sum_{j=1}^{N} w_j\, Y_{\ell m}^{*}(\Omega_j), \tag{16}$$

where w_j is the weight of the jth beam. We define the total weight by

$$W \equiv \sum_{j=1}^{N} w_j. \tag{17}$$

For the icosahedral orbit construction with K seeds, one has $N = 60K$. Unless otherwise noted, all numerical examples in this paper use equal weights $w_j = 1$, so that $W = N$.

3.1. Flat-top profile

We first consider the flat-top profile, which is constant within a cone of half-angle θ_{b} about the beam axis and vanishes outside it. The normalized profile is

$$b(\gamma) = \begin{cases} \dfrac{1}{2\pi(1-\cos\theta_{\mathrm{b}})}, & 0 \leq \gamma \leq \theta_{\mathrm{b}}, \\ 0, & \theta_{\mathrm{b}} < \gamma \leqslant \pi. \end{cases} \tag{18}$$

Let $\mu_0 = \cos\theta_\mathrm{b}$. Then, for $\ell \geq 1$, the transfer coefficients are

$$B_\ell = \frac{1}{1-\mu_0}\int_{\mu_0}^{1} P_\ell(\mu)\,\mathrm{d}\mu = \frac{P_{\ell-1}(\mu_0) - P_{\ell+1}(\mu_0)}{(2\ell+1)(1-\mu_0)}. \quad (19)$$

This profile provides a simple reference model with a sharp angular cutoff.

3.2. vMF profile

We next consider the axisymmetric vMF profile [36, 37], parameterized by a concentration parameter κ,

$$b(\gamma) = \frac{\exp(\kappa\cos\gamma)}{4\pi\,\mathrm{i}_0(\kappa)}, \quad (20)$$

where $\mathrm{i}_\ell(\kappa)$ denotes the modified spherical Bessel function. In particular,

$$\mathrm{i}_0(\kappa) = \frac{\sinh\kappa}{\kappa}. \quad (21)$$

The corresponding transfer coefficients are

$$B_\ell = \frac{\mathrm{i}_\ell(\kappa)}{\mathrm{i}_0(\kappa)}. \quad (22)$$

To express the beam width in the same form as for the flat-top profile, we parameterize κ by the half-maximum angle θ_b defined through $b(\theta_\mathrm{b}) = \frac{1}{2}b(0)$. This gives

$$\kappa = \frac{\ln 2}{1-\cos\theta_\mathrm{b}}. \quad (23)$$

In the narrow-beam limit $\gamma \ll 1$ and $\kappa \gg 1$, the normalized vMF profile approaches

$$b(\gamma) \simeq \frac{\kappa}{2\pi}\exp\left(-\frac{\kappa\gamma^2}{2}\right), \quad (24)$$

with angular variance $\sigma^2 \simeq 1/\kappa$. This profile provides a smooth Gaussian-like model on the sphere while preserving exact spherical normalization for any beam width.

Figure 1 compares the transfer coefficient B_ℓ for these two beam models. Here, $f = 2\sin\theta_\mathrm{b}$ is used as a common normalized spot-size parameter. For the vMF profile, θ_b is defined through the half-maximum condition and therefore corresponds to a full width at half maximum on the sphere. For the flat-top profile, the same parameter instead represents the full angular diameter. The flat-top case is retained mainly as a sharp-edge reference model, whereas the vMF profile serves as a smooth spherical model that is more representative of reactor-relevant spots. Both profiles are idealized, and a more detailed treatment of realistic focal-spot smoothing and plasma transport is left for future work. Owing to its sharp angular cutoff, the flat-top profile exhibits oscillatory behavior at large ℓ, whereas the vMF profile shows a smooth decay. In both cases, increasing the normalized spot size f filters out higher-degree spherical harmonics and shifts the spectral weight toward lower-degree modes.

4. Numerical method for σ_rms with transfer coefficients

4.1. Delta-function limit

Let $\{\Omega_j\}_{j=1}^N$ denote the set of beam-axis directions on the unit sphere. In the delta-function limit, the deposited intensity is represented as a sum of point contributions,

$$I_\delta(\Omega) = \sum_{j=1}^{N} w_j\,\delta(\Omega,\Omega_j), \quad (25)$$

where $\delta(\Omega,\Omega_j)$ is the Dirac delta distribution on S^2, and w_j is the weight of the jth beam. Expanding I_δ in orthonormal spherical harmonics gives

$$I_\delta(\Omega) = \sum_{\ell=0}^{\infty}\sum_{m=-\ell}^{\ell} a_{\ell m}^{(\delta)}\,Y_{\ell m}(\Omega), \quad (26)$$

with coefficients

$$a_{\ell m}^{(\delta)} = \int_{S^2} I_\delta(\Omega)\,Y_{\ell m}^*(\Omega)\,\mathrm{d}\Omega = \sum_{j=1}^{N} w_j\,Y_{\ell m}^*(\Omega_j). \quad (27)$$

Using equation (17), the monopole coefficient is

$$a_{00}^{(\delta)} = \frac{W}{\sqrt{4\pi}}. \quad (28)$$

Thus, in the point-beam limit, the spherical-harmonic content is determined entirely by the weighted angular distribution of the beam axes.

4.2. Finite-width beams and transfer coefficients

For an axisymmetric single-beam profile $b(\gamma)$ normalized as in the previous subsection, the deposited intensity is represented as a superposition of rotated copies,

$$I(\Omega) = \sum_{j=1}^{N} w_j\,b(\gamma(\Omega,\Omega_j)), \quad (29)$$

where $\cos\gamma(\Omega,\Omega_j) = \Omega\cdot\Omega_j$. The Legendre expansion of $b(\gamma)$ implies that each spherical-harmonic degree is filtered by the transfer coefficient B_ℓ. The spherical-harmonic coefficients, therefore, take the form

$$a_{\ell m} = B_\ell\,a_{\ell m}^{(\delta)} = B_\ell\sum_{j=1}^{N} w_j\,Y_{\ell m}^*(\Omega_j), \quad (30)$$

so that the delta-function limit corresponds to $B_\ell = 1$ for all ℓ.

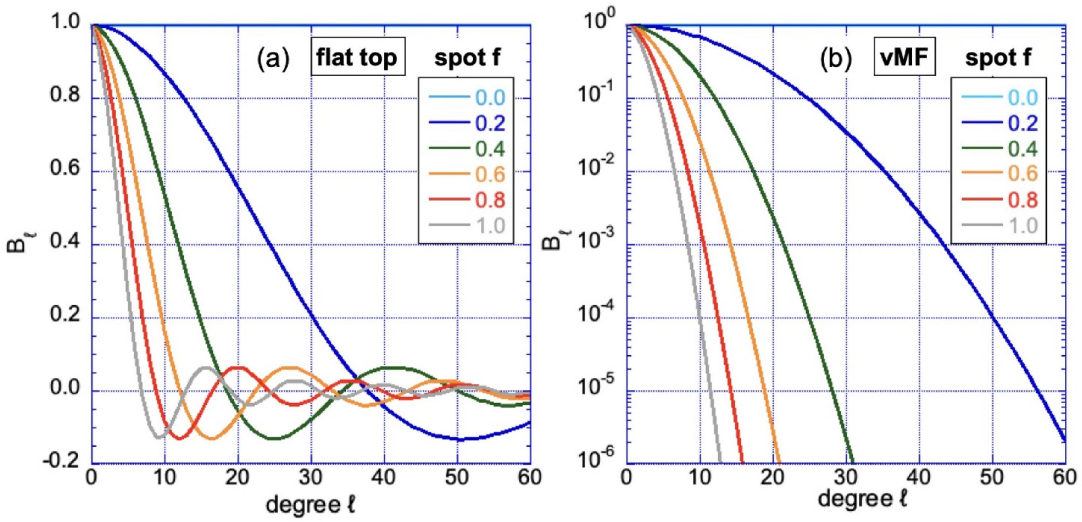


Figure 1. Transfer coefficients B_ℓ for several normalized spot sizes $f = 2\sin\theta_\mathrm{b}$, where f denotes the laser spot diameter normalized by the target diameter. (*a*) Flat-top profile. The sharp angular cutoff produces oscillatory behavior at large ℓ. (*b*) von Mises–Fisher (vMF) profile. The smooth profile yields a correspondingly smooth decay with increasing ℓ.

4.3. Implementation with real and imaginary parts

In the implementation, we store the real and imaginary parts of the complex coefficients for $m \geqslant 0$ as arrays $a^{\mathrm{re}}_{\ell m}$ and $a^{\mathrm{im}}_{\ell m}$. For each beam-axis direction $\Omega_j \equiv (\theta_j, \phi_j)$, we evaluate

$$\begin{aligned} \Re Y_{\ell m}(\Omega_j) &= N_{\ell m} p^m_\ell(\cos\theta_j)\cos(m\phi_j), \\ \Im Y_{\ell m}(\Omega_j) &= N_{\ell m} p^m_\ell(\cos\theta_j)\sin(m\phi_j), \end{aligned} \tag{31}$$

where

$$N_{\ell m} = \sqrt{\frac{2\ell+1}{4\pi}\frac{(\ell-m)!}{(\ell+m)!}} \tag{32}$$

includes the Condon–Shortley phase through the associated Legendre functions. We denote these functions by $p^m_\ell(\cos\theta)$ to avoid confusion with the power spectrum $\mathcal{P}_\ell$.

The code first accumulates the weighted geometric sums over beam directions and then applies the transfer coefficient B_ℓ degree by degree, i.e.

$$\begin{aligned} a^{\mathrm{re}}_{\ell m} &= B_\ell \sum_{j=1}^{N} w_j \Re Y_{\ell m}(\Omega_j), \\ a^{\mathrm{im}}_{\ell m} &= B_\ell \sum_{j=1}^{N} w_j \Im Y_{\ell m}(\Omega_j), \qquad (m \geqslant 0). \end{aligned} \tag{33}$$

Thus, the stored coefficients already include the finite-width filtering by B_ℓ.

The degree-resolved power spectrum is evaluated in the implementation as

$$\mathcal{P}_\ell = (a^{\mathrm{re}}_{\ell 0})^2 + 2\sum_{m=1}^{\ell}\left[(a^{\mathrm{re}}_{\ell m})^2 + (a^{\mathrm{im}}_{\ell m})^2\right]. \tag{34}$$

This expression is equivalent to equation (2) after using the $\pm m$ symmetry of the spherical-harmonic coefficients.

By the spherical-harmonic addition theorem, the same quantity can be written purely in terms of pairwise angular separations,

$$\mathcal{P}_\ell = \frac{2\ell+1}{4\pi}|B_\ell|^2 \sum_{i=1}^{N}\sum_{j=1}^{N} w_i w_j P_\ell(\Omega_i \cdot \Omega_j), \tag{35}$$

which corresponds to the geometrical-factor formulation introduced by Skupsky and Lee [11].

4.4. Power spectrum and σ_{rms}

Using $B_0 = 1$ together with $a_{00} = W/\sqrt{4\pi}$, the RMS nonuniformity is given by

$$\sigma^2_{\mathrm{rms}} = \frac{4\pi}{W^2}\sum_{\ell \geqslant 1}|B_\ell|^2 \sum_{m=-\ell}^{\ell}\left|\sum_{j=1}^{N} w_j Y^*_{\ell m}(\Omega_j)\right|^2. \tag{36}$$

Equivalently, if one defines the geometric power spectrum in the delta-function limit by

$$\mathcal{P}^{(\delta)}_\ell = \sum_{m=-\ell}^{\ell}|a^{(\delta)}_{\ell m}|^2, \tag{37}$$

then

$$\sigma^2_{\mathrm{rms}} = \frac{4\pi}{W^2}\sum_{\ell \geqslant 1}|B_\ell|^2 \mathcal{P}^{(\delta)}_\ell. \tag{38}$$

In the numerical optimization, the low-degree contributions to σ_{rms} are controlled both by geometric cancellation in the sums over Ω_j and by the profile-dependent filtering provided by B_ℓ.

4.5. Numerical optimization method

The optimized icosahedral layouts are constructed from K generic seed directions on the unit sphere. For each seed direction, the full set of beam axes is generated by applying all 60 proper rotations of the rotational icosahedral group I. We denote the resulting configuration by Ic_N, where $N = 60K$ is the total number of beam axes. For example, Ic_{60} corresponds to a single generic seed orbit generated by the 60 rotations of I.

Seed directions located exactly on symmetry axes of the icosahedral group are excluded from the optimization. For such special seed positions, some rotations leave the seed invariant or map it onto a previously generated direction. As a result, the group orbit contains fewer than 60 distinct beam axes and does not represent a generic Ic_N configuration with $N = 60K$ independent directions. To keep the beam number and symmetry construction well defined, only off-axis seeds that generate full 60-element orbits are used as optimization variables.

The optimization variables are the angular coordinates of the K seed directions. For a given trial set of seeds, the full beam set is first generated. The spherical-harmonic coefficients, angular power spectrum $\mathcal{P}_\ell$, and σ_{rms} are then evaluated for the specified beam profile, spot size, and beam weights. For the smooth vMF profiles emphasized in this paper, the results are only weakly sensitive to further increases in $\ell_{\max}$ because the transfer coefficients suppress the high-degree spectrum rapidly. The flat-top case is retained primarily as a reference model. In that case, the quantitative value of σ_{rms} can depend more strongly on the chosen truncation because of the slower decay of the high-degree spectrum.

The search itself is performed by repeated random perturbations of the seed directions. For each trial perturbation, σ^2_{rms} is evaluated from the angular power spectrum. The perturbation is accepted when σ^2_{rms} decreases and rejected otherwise. This procedure is iterated until no further substantial reduction is obtained. Because this is a stochastic local-improvement search, the final result can depend on the initial seeds. To reduce that sensitivity, many random initial conditions are tested and the configuration with the smallest converged value of σ^2_{rms} is retained. We therefore do not claim a rigorous proof of global optimality. For configurations with σ_{rms} at or below the 10^{-4} level, residual numerical and optimization uncertainties may produce relative variations of order 100% in the reported value. Nevertheless, repeated convergence from many starting conditions substantially reduces the likelihood that the reported Ic_N layouts are artifacts of a single unfavorable initialization.

5. Comparison between Ic_{60} and Ω_{60}

We next compare Ic_{60} with the actual OMEGA 60-beam pointing geometry, denoted Ω_{60}. The OMEGA geometry has been widely used as a reference configuration for direct-drive implosions [12, 13, 38, 39]. The present comparison is between a layout generated from the full rotational icosahedral group and the actual OMEGA pointing geometry. The purpose of this comparison is not to reproduce the full on-target uniformity of the OMEGA facility, which depends on measured focal spots, beam balance, smoothing by spectral dispersion, CBET, and plasma response. Rather, it isolates the geometrical contribution of the beam-axis distribution under common idealized beam profiles. Accordingly, throughout this section, statements that Ic_{60} is more favorable than Ω_{60} refer specifically to the spherical-harmonic nonuniformity metric used here for the beam-axis distribution, and not to a universal ordering of the two layouts under all possible geometrical or facility-level criteria.

The comparison is carried out in terms of the degree-resolved nonuniformity spectrum and the resulting σ_{rms}. Since the preceding sections showed that σ_{rms} is determined by the geometrical spectrum together with the profile-dependent transfer coefficients B_ℓ, this comparison makes it possible to separate purely geometrical effects from beam-profile effects. The single-beam profile itself is still idealized in the present study. OMEGA-specific super-Gaussian spot models are not used here. Instead, the comparison is made between a sharp-edge flat-top reference model and a smooth vMF model, with a super-Gaussian case expected to lie between these limiting cases.

Figures 2(a) and (d) shows the spectra in the delta-function limit, corresponding to $f = 0$. In this limit, the spectrum directly reflects the underlying weighted point set on the sphere, without additional filtering by finite beam width. The difference between the two configurations is already evident at this stage. The Ic_{60} spectrum exhibits exact zeros at the selected low spherical-harmonic degrees discussed in section 2. These vanishing amplitudes arise from algebraic cancellations enforced by the full icosahedral group. Thus, the Ic_{60} construction removes selected low-degree nonuniformity modes at the level of the beam geometry itself.

The conventional Ω_{60} layout shows a different type of symmetry. Its most characteristic feature is the presence of antipodal beam pairs, which, for equal beam weights, causes all odd-degree modes to vanish identically, as follows from equation (35). This property is clearly visible in figure 2(d). The cancellation of odd modes automatically lowers the total nonuniformity and reduces σ_{rms} by a factor of about $1/\sqrt{2}$ relative to a comparable spectrum in which odd- and even-degree contributions have similar weight. However, this symmetry alone does not suppress the even low-degree modes in the same systematic manner as the Ic_{60} construction. In this sense, Ω_{60} has a favorable parity symmetry, but it does not exhibit the same systematic suppression of low-degree modes as Ic_{60}.

The practical significance of this difference depends strongly on the beam profile through the transfer coefficients B_ℓ. We first consider the vMF profile at $f = 0.8$, shown in figures 2(b) and (e). Because the vMF transfer coefficients decay rapidly with increasing ℓ, high-degree modes are strongly attenuated, and the final nonuniformity is governed mainly by the remaining low-degree part of the spectrum. This is precisely the regime in which the geometrical structure becomes most important.

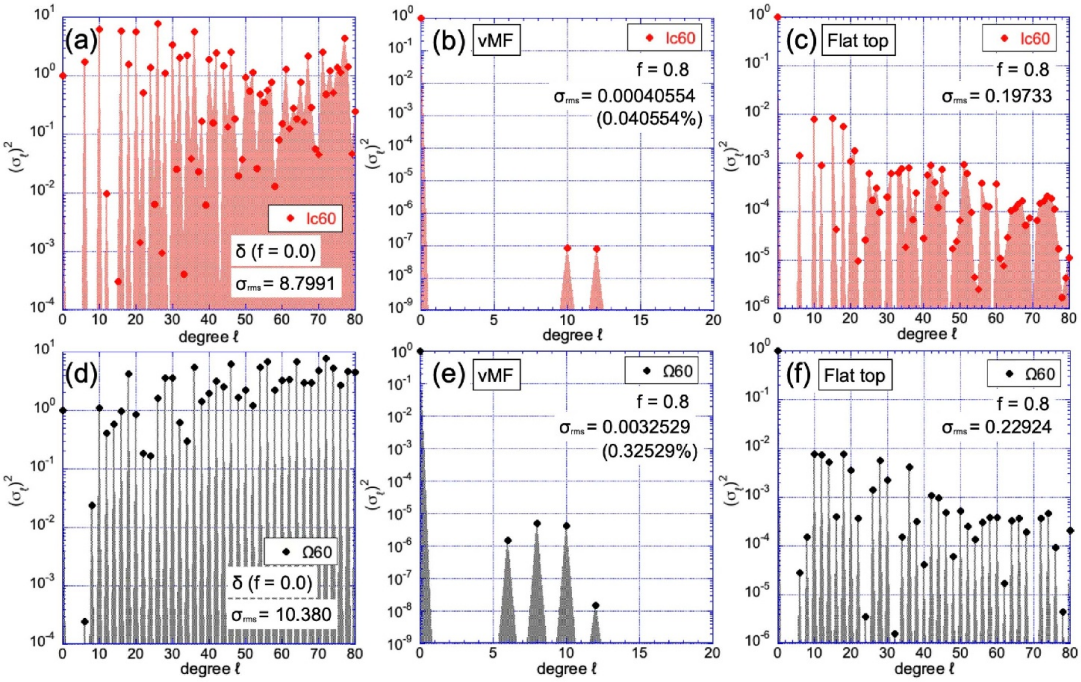


Figure 2. Degree-ℓ-resolved nonuniformity spectra for the optimized Ic_{60} layout and the Ω_{60} layout at $N = 60$. Panels (*a*) and (*d*) show the delta-function limit with $f = 0$. Panels (*b*) and (*e*) show the von Mises–Fisher (vMF) profile at $f = 0.8$. Panels (*c*) and (*f*) show the flat-top profile at $f = 0.8$. Panels (*a*)–(*c*) correspond to Ic_{60}, and panels (*d*)–(*f*) correspond to Ω_{60}.

For Ic_{60}, the selected low-degree modes are already zero in the delta-function limit. Once the finite beam width is introduced, the vMF profile suppresses the higher-degree modes as well, so that both low- and high-degree nonuniform components are simultaneously reduced. Consequently, the resulting σ_{rms} becomes extremely small, as shown in figure 2(*b*). In this case, the geometrical selection rule and the spectral filtering by B_ℓ act cooperatively.

The behavior of Ω_{60} at the same spot size is qualitatively different. As seen in figure 2(*e*), the odd modes are absent, and the lowest surviving amplitudes remain relatively small. The first nonzero contributions appear around $\ell = 6$, and the low-degree spectrum is modest. However, these low-degree components are not canceled in the same exact way as in Ic_{60}, and substantial even-degree contributions remain. In particular, the surviving even-degree modes around $\ell = 8$ and $\ell = 10$ contribute appreciably to the total nonuniformity. As a result, although Ω_{60} already yields a relatively small σ_{rms}, the Ic_{60} configuration gives a significantly smaller calculated σ_{rms} for the vMF profile within the present spherical-harmonic nonuniformity metric for the beam-axis distribution. At $f = 0.8$, the Ic_{60} value is about one order of magnitude smaller than that of Ω_{60}.

A rather different trend is found for the flat-top profile. Figures 2(*c*) and (*f*) compares Ic_{60} and Ω_{60} at $f = 0.8$ for this beam model. In this case, the spectra of the two configurations remain much more similar. The reason is that the flat-top profile does not suppress high-degree modes efficiently. Because of the sharp beam edge, the corresponding transfer coefficients decay slowly and oscillate, so that substantial high-degree spectral power survives even at large spot size. Therefore, although Ic_{60} still retains the mathematically important property that selected low-degree modes are exactly zero, the remaining higher-degree modes continue to contribute significantly to the total nonuniformity. The same is true for Ω_{60}. Although the odd modes are canceled by antipodal pairing, many even higher-degree modes remain. Consequently, neither configuration exhibits the dramatic reduction in σ_{rms} seen for the vMF case.

This overall behavior is summarized in figure 3, which plots σ_{rms} as a function of normalized spot size f for both layouts and both beam profiles. For the vMF profile, Ic_{60} shows a clear and systematic advantage over Ω_{60}, and the difference becomes especially pronounced at large spot size, reaching about one order of magnitude near $f = 0.8$. By contrast, for the flat-top profile, the two curves remain close over a broad range of f, and around $f \sim 0.7$ the Ic_{60} value can even become slightly larger than that of Ω_{60}. Thus, the superiority of Ic_{60} in the calculated σ_{rms} is not universal for all beam profiles. Rather, it emerges most strongly when the beam profile efficiently removes the higher-degree modes that are not canceled geometrically.

The comparison also clarifies the mathematical role of the present optimization. The advantage of Ic_{60} is not merely an empirical reduction of the overall nonuniformity, but the exact cancellation of selected low-degree nonuniformity modes enforced by full rotational icosahedral invariance. Although Ω_{60} is already a highly symmetric configuration, its symmetry is reflected primarily in the cancellation of odd-degree modes

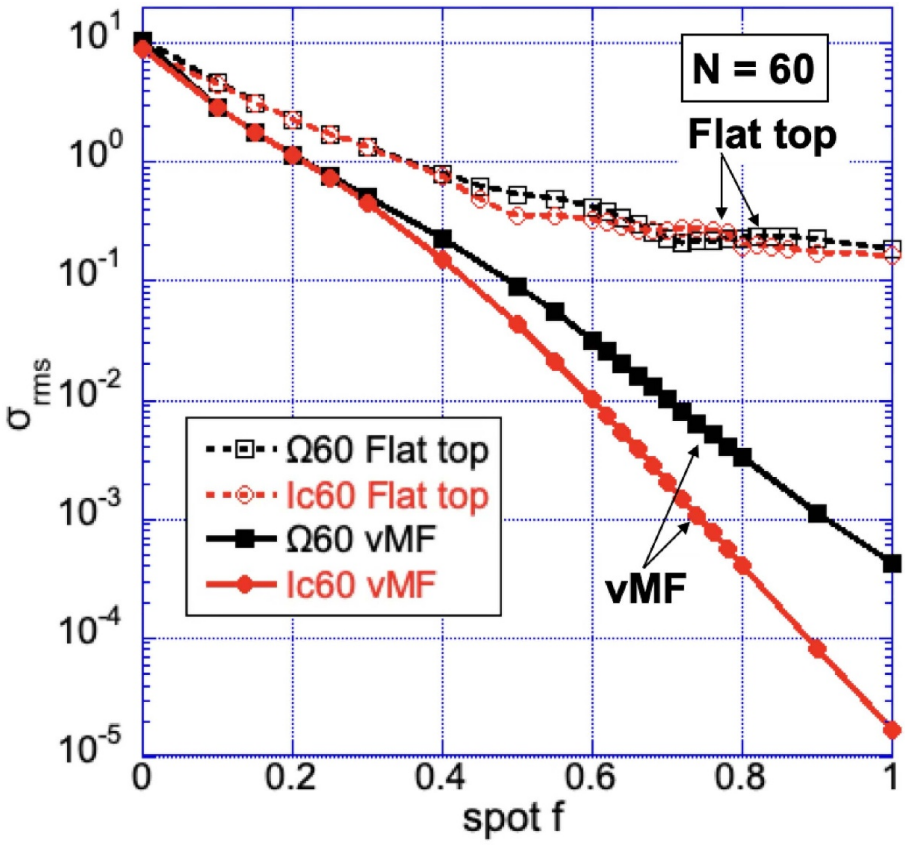


Figure 3. RMS nonuniformity $\sigma_{\rm rms}$ as a function of normalized spot size f for Ic_{60} and Ω_{60} at $N = 60$, for flat-top and von Mises–Fisher (vMF) beam profiles.

by antipodal pairing, and it does not impose the same icosahedral selection rules on the low-degree spectrum. In this sense, the Ic_{60} construction more fully exploits the cancellation capability of the icosahedral group.

The practical gain from this geometrical cancellation is realized most strongly when it is combined with a beam profile that suppresses the remaining high-degree spectrum. The icosahedral selection rules remove selected low-degree modes, while the transfer coefficients B_ℓ of a smooth beam profile attenuate the residual high-degree modes. Consequently, Ic_{60} yields substantially higher irradiation uniformity than Ω_{60} for the vMF profile, whereas the advantage is weaker for the flat-top profile because the sharp edge leaves significant high-degree power. This leads to the design principle that geometrical low-mode cancellation and profile-based high-mode suppression should be optimized together.

6. Sensitivity to weight imbalance

We next examine the sensitivity of the irradiation nonuniformity to beam-to-beam weight imbalance. In the preceding calculations, all beams were assigned equal weights. Here, the equal-weight condition is relaxed by introducing beam-dependent weights.

For each beam, a provisional weight is first assigned as

$$\tilde{w}_i = 1 + \Delta_w (2r_i - 1), \qquad r_i \sim \mathcal{U}(0,1), \tag{39}$$

where $\mathcal{U}(0,1)$ denotes the uniform distribution on the interval $[0,1]$. Thus, $2r_i - 1$ is uniformly distributed over $[-1,1]$, and Δ_w specifies the imposed fractional amplitude of the beam-weight imbalance before normalization. The provisional weights therefore satisfy

$$1 - \Delta_w \leqslant \tilde{w}_i \leqslant 1 + \Delta_w. \tag{40}$$

The provisional weights are then multiplied by a common normalization factor,

$$w_i = \frac{N\tilde{w}_i}{\sum_{j=1}^{N} \tilde{w}_j}. \tag{41}$$

This normalization gives

$$\sum_{i=1}^{N} w_i = N, \tag{42}$$

so that the total beam weight is the same as in the equal-weight case. The irradiation profile and the corresponding nonuniformity are then evaluated using the normalized weights w_i.

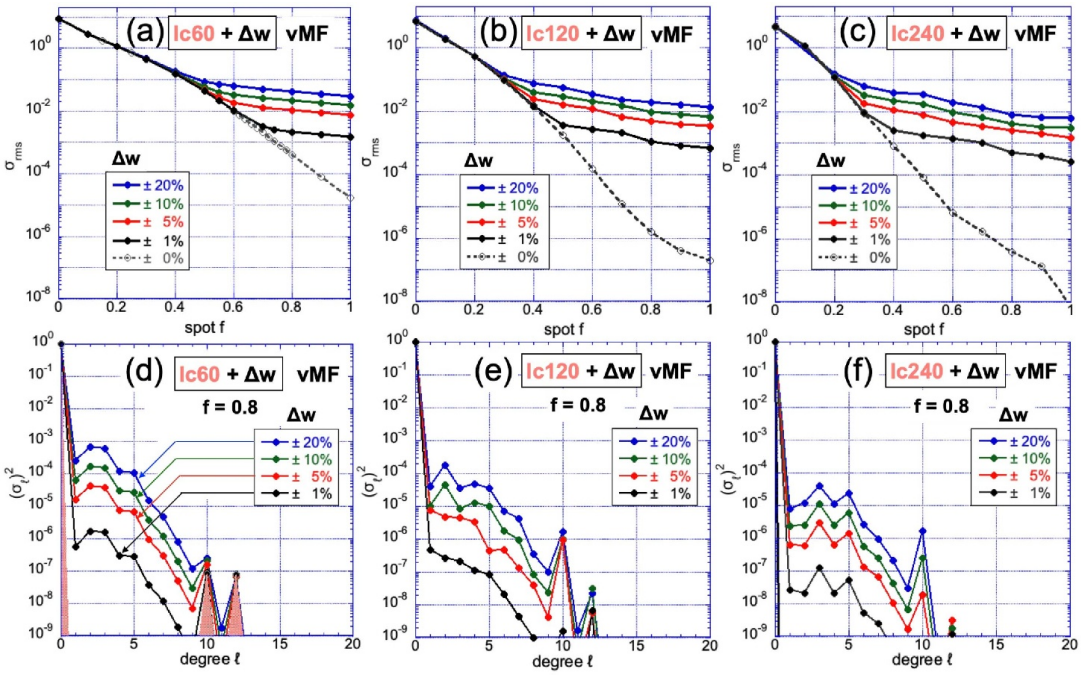


Figure 4. Effect of random beam-weight imbalance on the optimized Ic_{60}, Ic_{120}, and Ic_{240} layouts for the von Mises–Fisher beam profile. Panels (*a*)–(*c*) show the RMS nonuniformity σ_{rms} as a function of the normalized spot size f for Ic_{60}, Ic_{120}, and Ic_{240}, respectively. The curves include the equal-weight case and random beam-weight variations with nominal amplitudes $\Delta_w = \pm 1\%$, $\pm 5\%$, $\pm 10\%$, and $\pm 20\%$ before total-weight normalization. Panels (*d*)–(*f*) show the corresponding degree-resolved spectra for the vMF profile at $f = 0.8$.

Figure 4 shows the change in RMS nonuniformity when random beam-weight imbalance is imposed. Figures 4(*a*)–(*c*) show σ_{rms} as a function of the normalized spot size f for Ic_{60}, Ic_{120}, and Ic_{240}, respectively. For small f, the curves with finite Δ_w are close to the equal-weight result. As f is increased, the difference from the equal-weight case becomes much larger. The wider-beam region is therefore more sensitive to beam-to-beam weight variations.

In the equal-weight case, $\Delta_w = 0$, the larger-f region shows an even stronger dependence on beam number, and σ_{rms} decreases with increasing beam number. The reduction is not uniform over the range of N shown here. In particular, at $f = 0.8$, the decrease from Ic_{60} to Ic_{120} is very large, and σ_{rms} is reduced to approximately 2^{-8} of its Ic_{60} value. This corresponds to a reduction of more than two orders of magnitude. The further reduction from Ic_{120} to Ic_{240} is more modest, and is approximately a factor of two.

The strong reduction observed in the equal-weight case shows a feature similar to that discussed by Shvydky *et al* [40] for spherical t-design beam configurations. In a spherical t-design, the beam directions are arranged so that low-degree angular components are strongly suppressed under equal weighting. The equal-weight curves obtained here show a similar tendency. When the beam profile is sufficiently wide, the geometrical contribution to the irradiation nonuniformity can be reduced by orders of magnitude as the beam number is increased.

The results for finite Δ_w further show that σ_{rms} can be reduced by decreasing the amplitude of the beam-weight imbalance. For a fixed beam number, the increase in σ_{rms} is approximately proportional to the imposed imbalance amplitude Δ_w over the range shown in figures 4(*a*)–(*c*). At the same values of f and Δ_w, σ_{rms} is smaller for a larger beam number. This reduction is clearly seen when comparing Ic_{60}, Ic_{120}, and Ic_{240}. For finite Δ_w, the values of σ_{rms} in the wider-beam region decrease approximately in proportion to N^{-1} over the range $N = 60$–240.

Figures 4(*d*)–(*f*) show the corresponding degree-resolved spectra for the vMF profile at $f = 0.8$. As shown in figure 2, in the equal-weight case, the dominant remaining components appear mainly around geometrical modes such as $\ell = 10$ and $\ell = 12$. When Δ_w is finite, additional low-degree components appear. In particular, the modes from $\ell = 1$ to $\ell = 9$ become nonzero, and large peaks are often observed around $\ell = 2$ or $\ell = 3$. These newly generated low-degree components are the main reason why the σ_{rms} becomes larger than in the equal-weight case at large f.

As the number of beams is increased, most of the low-degree components generated by beam-weight imbalance are reduced. On the other hand, the geometrical components already present in the equal-weight case do not necessarily follow the same trend. When random beam-weight imbalance is present, increasing the number of beams can cause some of the modes already present in the equal-weight case to increase

slightly. For example, the component near $\ell = 10$ can become slightly larger as N is increased in the present calculations.

Figure 5 summarizes the beam-number dependence more directly. For the wider-beam case, $f = 0.8$, the finite-imbalance cases initially decrease approximately as N^{-1} over the low-to-intermediate beam-number range. After about $N \sim 500$, however, the slopes become steeper; for $N > 1000$, the decrease can be regarded as closer to an N^{-2} trend than to an N^{-1} trend. Thus, the important result is not a single N^{-1} scaling over the entire range, but a systematic steepening of the beam-number dependence in optimized high-beam-count icosahedral layouts. This behavior is distinct from the $N^{-1/2}$ trend expected from uncorrelated random sampling of independent beam directions.

The origin of this stronger reduction is that the beam directions are not random points on the sphere. They are organized into complete icosahedral orbits whose equal-weight low-degree moments are exactly canceled or strongly suppressed. Beam-weight errors, therefore, perturb an already symmetry-canceled spectrum, and the fractional contribution carried by each individual beam also decreases as the total beam number increases. As a result, the low-degree components produced by weight imbalance are reduced much more efficiently than in a random angular distribution.

The $f = 0.6$ case shows a different low-N behavior. At smaller N, the decrease is closer to an $N^{-1/2}$ trend than to an N^{-1} trend. This is because a narrower vMF beam has larger transfer coefficients at higher spherical-harmonic degrees, so higher-degree angular structure is less strongly filtered. For smaller f and smaller N, these residual high-degree components remain more important, and the imbalance-induced nonuniformity is therefore closer to the random-averaging behavior. As N is increased, the optimized icosahedral geometry suppresses a larger part of the relevant angular spectrum, and the dependence on N becomes steeper. In this respect, both $f = 0.6$ and $f = 0.8$ cases show a stronger beam-number dependence as N becomes large.

The comparison with spherical t-designs is useful for interpreting the equal-weight limit. Shvydky *et al* [40] showed that arranging beam directions according to a spherical t-design can strongly suppress irradiation nonuniformity under equal-weight conditions. The equal-weight results in figure 4 show the same kind of geometrical suppression, especially in the larger-f region. The present calculation extends this picture by examining how that cancellation is broken by unequal beam weights. A mode canceled by the equal-weight sum over beam axes is no longer guaranteed to vanish when the weights fluctuate, because the corresponding weighted sum contains the random perturbations of the individual beam powers.

Nevertheless, high-beam-count optimized geometry remains beneficial in the presence of weight imbalance. Increasing N reduces the fractional weight carried by each beam and distributes the weight errors over more symmetry-related directions. Thus, two distinct mechanisms are involved: exact or near-exact geometrical cancellation in the equal-weight limit, and reduction of the residual imbalance-induced modes through many-beam averaging on an optimized icosahedral layout. The results in figures 4 and 5 show that these two mechanisms work together to reduce the sensitivity to beam-weight imbalance.

These results indicate that increasing the number of beams improves the robustness of the irradiation uniformity against moderate beam-to-beam weight imbalance. For reactor-scale laser systems, where small beam-to-beam weight variations are difficult to eliminate completely, this redundancy is a practical advantage. The present calculation, therefore, supports the use of a large number of beams not only for improving the equal-weight irradiation uniformity, but also for reducing the sensitivity to realistic beam-weight variations.

Follett *et al* reported that, in their OMEGA-based surrogate design model, reducing the Rayleigh–Taylor (RT) seed amplitude by a factor of 10 can increase the target gain by about 50%, whereas recovery of the performance of the corresponding 1-D designs would require an approximately 1000-fold reduction in the RT seed level [41]. They also found that several laser-system upgrades, including increasing the number of drive beams from 60 to 720, can provide performance enhancements comparable to reducing the RT seed.

The connection between irradiation nonuniformity and the hydrodynamic seed can be expressed in terms of the ablation-pressure response. If the local ablation pressure P_{a} scales as the αth power of the laser intensity I,

$$P_{\mathrm{a}} \propto I^{\alpha}, \tag{43}$$

then a small fractional intensity perturbation produces

$$\frac{\delta P_{\mathrm{a}}}{P_{\mathrm{a}}} = \alpha \frac{\delta I}{I}. \tag{44}$$

Thus, the irradiation nonuniformity $\delta I/I$ represents a direct upstream drive perturbation that produces ablation-pressure nonuniformity $\delta P_{\mathrm{a}}/P_{\mathrm{a}}$. For 351 nm direct-drive ablation, Fratanduono *et al* measured approximately $P_{\mathrm{a}} \propto I^{0.71}$, giving $\alpha \simeq 0.71$ [42]. The resulting pressure perturbation can generate shock, velocity, and shell-displacement perturbations, which act as hydrodynamic seeds for subsequent RT growth [43, 44].

Within this linear-response interpretation, the present σ_{rms} should be regarded as an illumination-side estimate of the laser-driven input to imprint and beam-mode hydrodynamic seeds, rather than as the total RT seed itself, because this estimate does not include other possible seed sources, such as target roughness, target offset, beam mistiming, stalk perturbations, polarization effects, or other target imperfections. If the laser-imprint component of the RT seed were dominant and scaled approximately linearly with the relevant irradiation nonuniformity spectrum, then a 1000-fold reduction from an OMEGA-level irradiation nonuniformity of order $\sigma_{\mathrm{rms}} \simeq 2\%$ [39] would correspond to an equivalent irradiation-uniformity level of approximately 2×10^{-5}. Based on figure 5, this equivalent level can be reached at about $N = 1920$ when the random weight perturbation is $\pm 1\%$. This result suggests that, if the laser-driven component of the seed is a dominant contribution, high-beam-count icosahedral irradiation could reduce the drive-induced seed to a level relevant to the RT-seed reductions discussed by Follett *et al*. This

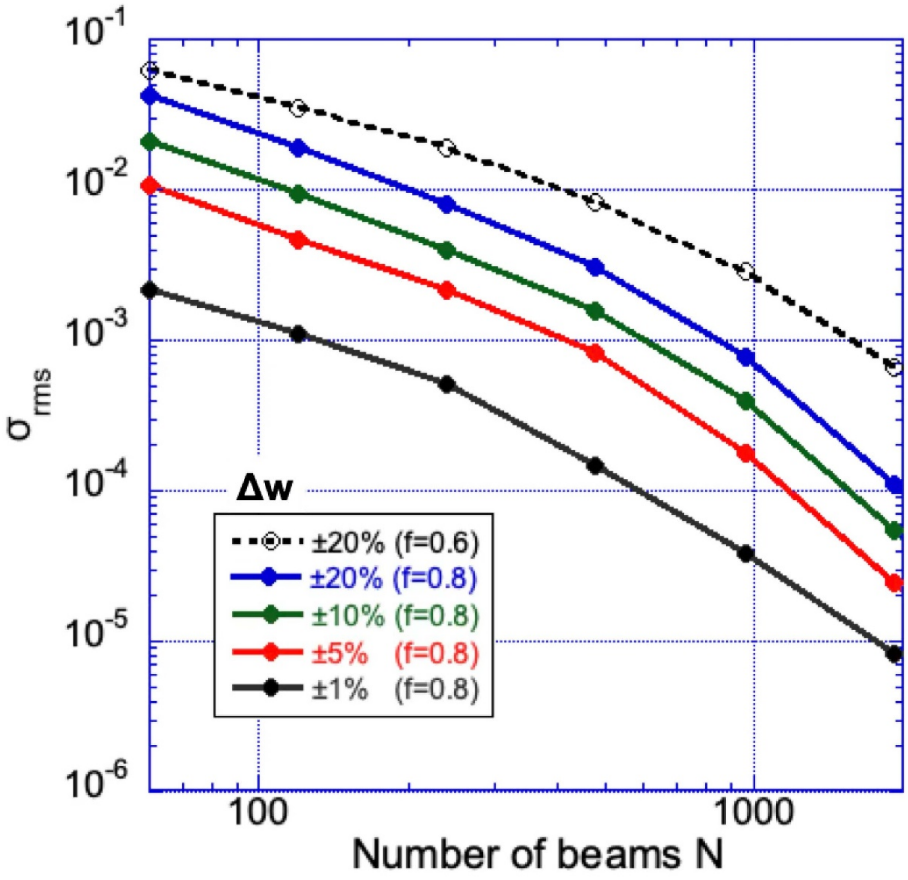


Figure 5. RMS nonuniformity $\sigma_{\rm rms}$ as a function of beam number N for optimized icosahedral layouts with the von Mises–Fisher beam profile. The figure shows the $f = 0.8$ cases for nominal beam-to-beam weight imbalance amplitudes of $\pm 20\%$, $\pm 10\%$, $\pm 5\%$, and $\pm 1\%$ before total-weight normalization. The $f = 0.6$, $\pm 20\%$ case is also shown for comparison. For $f = 0.8$, the finite-imbalance cases initially decrease approximately as N^{-1} at low-to-intermediate beam numbers, become steeper after about $N \sim 500$, and approach a roughly N^{-2} trend for $N > 1000$. The $f = 0.6$ case starts closer to an $N^{-1/2}$ trend and also steepens as N increases.

irradiation-uniformity requirement is complementary to other future direct-drive driver requirements, such as broadband-laser mitigation of laser–plasma instabilities discussed by Froula *et al* [22].

7. Conclusion

We have presented a symmetry-based framework for high irradiation uniformity in direct-drive laser fusion using beam layouts generated from the full rotational icosahedral group. The main results are as follows. First, exact icosahedral invariance imposes a strict selection rule on the spherical-harmonic spectrum: the degrees $\ell = 1, 2, 3, 4, 5, 7, 8, 9, 11, 13, 14, 17, 19, 23,$ and 29 are forbidden, and this statement remains valid for finite-width beams as well as in the delta-function limit. Second, the practical performance of the optimized layouts depends on the interplay between this symmetry-based low-mode suppression and the profile-dependent transfer coefficients that attenuate the remaining high-order spectrum. Third, the optimized Ic_{60} layout quantitatively outperforms the actual OMEGA 60-beam geometry for smooth beam profiles, while the advantage is smaller for a sharp-edge flat-top reference profile because higher-order modes remain important. Fourth, optimized Ic_N layouts remain robust against random beam-weight imbalance, with an approximately linear response to imbalance amplitude and a residual $\sigma_{\rm rms}$ that decreases approximately as $1/N$ at low-to-intermediate beam numbers for $f = 0.8$, steepens after about $N \sim 500$, and approaches a nearly $1/N^2$ trend for $N > 1000$ in the range examined here. These results extend our previous Opt. Express study [32] by providing an explicit spectral analysis, a direct comparison with the actual Ω_{60} geometry, and quantitative scaling results under beam-weight imbalance. By combining full icosahedral symmetry, smooth beam profiles, and a sufficiently large number of beams, irradiation nonuniformity can be reduced to levels relevant to ignition-class or reactor-class implosions.

At the same time, the present paper should be interpreted as establishing an illumination-geometry design principle rather than as a complete assessment of the effects of nonuniformity

on implosion performance. Hydrodynamic validation remains a necessary next step, and realistic target imperfections such as out-of-roundness, surface roughness, and other nonuniformity sources must also be included in a full reactor assessment [45]. Our model also omits intrabeam speckle, mutual coherence between beams, and optical-field statistics. These effects and optical smoothing techniques, such as those investigated by Lehmberg and Goldhar [46], remain topics for future work. Even with these caveats, the substantial reduction of drive nonuniformity demonstrated here is important for direct-drive fusion, because irradiation asymmetry is a primary source of implosion asymmetry and can also couple to laser–plasma-interaction physics through CBET, nonuniform absorption, and feedback on the coronal plasma conditions. The present icosahedral layouts, therefore, provide a promising and scalable basis for robust low-mode and RMS drive-nonuniformity control in future direct-drive fusion systems.

ORCID iDs

Atsushi Sunahara 0000-0001-7543-5226
Gaurav Raj 0000-0003-3565-7769

References

[1] Nuckolls J., Wood L., Thiessen A. and Zimmerman G. 1972 Laser compression of matter to super-high densities: thermonuclear (CTR) applications *Nature* **239** 139–42
[2] Lindl J.D. 1998 *Inertial Confinement Fusion: The Quest for Ignition and Energy Gain Using Indirect Drive* (AIP Press/Springer)
[3] Atzeni S. and Meyer-ter-Vehn J. 2004 *The Physics of Inertial Fusion: Beam Plasma Interaction, Hydrodynamics, Hot Dense Matter* (Clarendon)
[4] Thomson J.J. 1904 On the structure of the atom: an investigation of the stability and periods of oscillation of a number of corpuscles arranged at equal intervals around the circumference of a circle; with application of the results to the theory of atomic structure *Phil. Mag.* **7** 237–65
[5] Delsarte P., Goethals J.M. and Seidel J.J. 1977 Spherical codes and designs *Geom. Dedicata* **6** 363–88
[6] Scott R.H.H. *et al* 2013 Numerical modeling of the sensitivity of x-ray driven implosions to low-mode flux asymmetries *Phys. Rev. Lett.* **110** 075001
[7] Mohamed Z.L. *et al* 2024 Demonstration of low-mode shape control in indirect-drive double shell implosions at the NIF *Phys. Plasmas* **31** 052701
[8] Ralph J.E. *et al* 2024 The impact of low-mode symmetry on inertial fusion energy output in the burning plasma state *Nat. Commun.* **15** 2975
[9] Abu-Shawareb H. *et al* 2024 Achievement of target gain larger than unity in an inertial fusion experiment *Phys. Rev. Lett.* **132** 065102
[10] Pak A. *et al* 2024 Observations and properties of the first laboratory fusion experiment to exceed a target gain of unity *Phys. Rev.* E **109** 025203
[11] Skupsky S. and Lee K. 1983 Uniformity of energy deposition for laser driven fusion *J. Appl. Phys.* **54** 3662–71
[12] Boehly T.R. *et al* 1992 The upgrade to the OMEGA laser system *Proc. SPIE* **1627** 236–45
[13] Boehly T.R. *et al* 1997 Initial performance results of the OMEGA laser system *Opt. Commun.* **133** 495–506
[14] McCrory R.L. *et al* 2001 OMEGA ICF experiments and preparation for direct drive ignition on NIF *Nucl. Fusion* **41** 1413–22
[15] Mannion O.M. *et al* 2021 Mitigation of mode-one asymmetry in laser-direct-drive inertial confinement fusion implosions *Phys. Plasmas* **28** 042701
[16] Goncharov V.N. *et al* 2017 National direct-drive program on OMEGA and the National Ignition Facility *Plasma Phys. Control. Fusion* **59** 014008
[17] Edgell D., Lees A., Shah R., Shvydky A. and Turnbull D. 2025 Low-mode nonuniformity in direct-drive ICF implosions due to laser smoothing techniques employed on OMEGA *Phys. Plasmas* **32** 102701
[18] Trickey W., Cao D., Marozas J.A., Shah R., Shvydky A., Collins T.J.B. and Goncharov V.N. 2026 Design options for achieving burning plasma and gain for next-generation laser direct-drive facilities *Phys. Plasmas* **33** 052707
[19] Davis A.K. *et al* 2016 Isolating and quantifying cross-beam energy transfer in direct-drive implosions on OMEGA and the National Ignition Facility *Phys. Plasmas* **23** 056306
[20] Edgell D.H., Hansen A.M., Katz J., Turnbull D. and Froula D.H. 2021 Unabsorbed light beamlets for diagnosing coronal density profiles and absorption nonuniformity in direct-drive implosions on OMEGA *Rev. Sci. Instrum.* **92** 043525
[21] Nguyen K.L., Yin L., Albright B.J., Edgell D.H., Follett R.K., Turnbull D., Froula D.H. and Palastro J.P. 2023 Cross-beam energy transfer in conditions relevant to direct-drive implosions on OMEGA *Phys. Plasmas* **30** 073901
[22] Froula D.H. *et al* 2025 A future of inertial confinement fusion without laser–plasma instabilities *Phys. Plasmas* **32** 052713
[23] Schmitt A.J. 1984 Absolutely uniform illumination of laser fusion pellets *Appl. Phys. Lett.* **44** 399–401
[24] McGeoch M.W. and Obenschain S.P. 2024 Direct drive laser fusion facility and pilot plant *J. Fusion Energ.* **43** 23
[25] Murakami M., Nishihara K. and Azechi H. 1993 Irradiation nonuniformity due to imperfections of laser beams *J. Appl. Phys.* **74** 802–8
[26] Murakami M. 1995 Irradiation system based on dodecahedron for inertial confinement fusion *Appl. Phys. Lett.* **66** 1587–9
[27] Murakami M., Sarukura N., Azechi H., Temporal M. and Schmitt A.J. 2010 Optimization of irradiation configuration in laser fusion utilizing self-organizing electrodynamic system *Phys. Plasmas* **17** 082702
[28] Murakami M. and Nishi D. 2017 Optimization of laser-driven microbubble implosion *Matter Radiat. Extremes* **2** 55–68
[29] Eimerl D. *et al* 2014 StarDriver: a flexible laser driver for inertial confinement fusion and high energy density physics *J. Fusion Energy* **33** 476–88
[30] Eimerl D. and Schmitt A.J. 2016 StarDriver: an estimate of the bandwidth required to suppress the $2\omega_{pe}$ instability *Plasma Phys. Control. Fusion* **58** 115006
[31] Eimerl D., Skupsky S., Myatt J. and Campbell E.M. 2016 A StarDriver-class laser achieving 1% beam uniformity in 1 ns *J. Fusion Energy* **35** 459–69
[32] Sunahara A., Raj G., Cohen T., Pattison P.M., Rudy P., Ohara Y., Iizuka S., Ohta H. and Nakamura S. 2025 Laser-based inertial fusion energy system enabled by optical enhancement cavities and a direct-drive configuration reactor *Opt. Express* **33** 47104–20
[33] Cohan N.V. 1958 The spherical harmonics with the symmetry of the icosahedral group *Proc. Camb. Phil. Soc.* **54** 28–38
[34] Meyer B. 1954 On the symmetries of spherical harmonics *Can. J. Math.* **6** 135–57
[35] Ahrens C. and Beylkin G. 2009 Rotationally invariant quadratures for the sphere *Proc. R. Soc.* A **465** 3103–25
[36] Fisher R.A. 1953 Dispersion on a sphere *Proc. R. Soc.* A **217** 295–305

[37] Banerjee A., Dhillon I.S., Ghosh J. and Sra S. 2005 Clustering on the unit hypersphere using von Mises–Fisher distributions *J. Mach. Learn. Res.* **6** 1345–82 (available at: https://jmlr.org/papers/v6/banerjee05a.html)
[38] Temporal M., Piriz A.R., Canaud B., Ramis R. and Craxton R.S. 2023 Partition of Omega-like facility into two configurations of 24 and 36 laser beams to improve implosion performance *Sci. Rep.* **13** 10010
[39] Sampat S., Kwiatkowski J., Heimbueger M., Ehrich B., Shvydky A., Waxer L.J. and Kruschwitz B.E. 2025 On-target uniformity of the OMEGA 60-beam inertial confinement fusion laser *Opt. Eng.* **64** 096102
[40] Shvydky A., Trickey W., Maximov A.V., Igumenshchev I.V., McKenty P.W. and Goncharov V.N. 2023 Optimization of irradiation configuration using spherical t-designs for laser-direct-drive inertial confinement fusion *Nucl. Fusion* **63** 014004
[41] Follett R.K. *et al* 2025 An experimentally informed design process for future inertial confinement fusion facilities *Phys. Plasmas* **32** 042705
[42] Fratanduono D.E., Boehly T.R., Celliers P.M., Barrios M.A., Eggert J.H., Smith R.F., Hicks D.G., Collins G.W. and Meyerhofer D.D. 2011 The direct measurement of ablation pressure driven by 351-nm laser radiation *J. Appl. Phys.* **110** 073110
[43] Craxton R.S. *et al* 2015 Direct-drive inertial confinement fusion: A review *Phys. Plasmas* **22** 110501
[44] Hu S.X., Fiksel G., Goncharov V.N., Skupsky S., Meyerhofer D.D. and Smalyuk V.A. 2012 Mitigating laser imprint in direct-drive inertial confinement fusion implosions with high-Z dopants *Phys. Rev. Lett.* **108** 195003
[45] Johnson T.M., Casey D.T., Weber C.R., Hurricane O.A., Nora R.C. and Davidovits S. 2026 Robustness of inertial fusion energy relevant implosions to low-mode asymmetries *Phys. Plasmas* **33** 072704
[46] Lehmberg R.H. and Goldhar J. 1987 Use of incoherence to produce smooth and controllable irradiation profiles with KrF fusion lasers *Fusion Technol.* **11** 532–41